STATIC AND DYNAMIC FIELD CHARACTERISATION OF THE SUPER PROTON SYNCHROTRON BENDING MAGNETS

A. Bellelli*[1,2], A. Ganesh[1], C. Petrone[1], M. Buzio[1], M. Bonora–Tam[1], A. Huschauer[1], S. Russenschuck[2]
[1]European Organization for Nuclear Research (CERN), Geneva, Switzerland
[2] Technische Universität Wien, Vienna, Austria

Abstract

To ensure precise control of field quality in normal-conducting accelerator magnets, it is essential to develop models that accurately represent magnetic hysteresis during operational cycles. This study focuses on the dipole magnets of the CERN Super Proton Synchrotron (SPS) and investigates how variations in operational cycles produce different hysteresis and dynamic patterns in the integrated main magnetic and higher-order field multipoles. A combination of various magnetic field measurement systems was employed to evaluate the magnetic field quality, enabling direct observation of history dependence and reproducibility. Three regimes are identified: a history-dependent reversal curve along the ramp, eddy-current settling during end-of-ramp transients, and a rate-independent transfer function at the plateau. The analysis covers the integrated dipole and sextupole components, distinguishing rate-dependent eddy current effects from quasi-static hysteretic contributions. Two pre-cycle patterns currently used in operation are compared: a 200 GeV cycle and a 26 GeV cycle introduced in 2026 within the CERN Efficient Particle Accelerator (EPA) initiative. The aim is to provide a quantitative single-magnet assessment of this change of operation.

INTRODUCTION

The Super Proton Synchrotron (SPS) at CERN relies on 744 main dipole magnets, of two types (MBA and MBB), to bend protons along its 6.9 km circumference. Besides serving as Large Hadron Collider (LHC) injector, the SPS delivers proton beams to the North Area fixed targets [1], where the dipolar B_1 and sextupolar B_3 field components directly drive orbit stability and beam quality at slow extraction. In normal-conducting magnets with time-varying magnetic field, two phenomena complicate the field description: (i) iron hysteresis, which introduces history-dependent static contributions, and (ii) eddy currents in the laminated yoke, end plates, and vacuum chamber, which produce rate-dependent dynamic effects. A real-time monitoring system (B-train) measures the magnetic fields of two reference dipoles, powered in series with the ring. Integrating over time the induced voltages from several pickup coils and periodically correcting the resulting flux measurement with a Nuclear Magnetic Resonance (NMR) field marker [2, 3], the system measures the integrated magnetic field, which serves as input to low-level radio-frequency (RF) and feed-forward correction [4, 5].

* alberto.bellelli@cern.ch

MOTIVATION

Current SPS operation uses a pre-cycle magnet excitation function, named MD1, before each SPS Fixed-Target PROton (SFTPRO) cycle for North Area experiments. The MD1 cycle was originally introduced to improve magnetic reproducibility and historically reached the equivalent of 200 GeV beam energy during the early LHC beam-scheduling era [6, 7]. In 2024, the presence of this cycle accounted for about 5 GWh of electrical energy consumption and 18 % of SPS operational time [4]. Following studies within the CERN Efficient Particle Accelerator (EPA) framework [1], the MD1 function was flattened at the beginning of 2026 to a 26 GeV plateau. This operational change motivates a quantitative assessment of how different magnetic histories affect the reproducibility and dynamic response of the SPS dipole magnets.

This work describes how the hysteretic response of the SPS dipole magnets has changed following the flattening of the MD1 cycle, and analyses their dynamic behaviour. To obtain this characterisation of the magnetic field response, a systematic measurement campaign was initiated in 2024, new instrumentation was developed, and a dedicated magnetic measurement procedure was implemented. This paper details the procedure, metrological characterisation, and measurement results.

MEASUREMENT METHODS

Measurement Setup

The measurements were performed on an MBA magnet, connected in series with an MBB laboratory reference dipole and driven by a voltage-controlled converter, with a reproducibility of 0.03 % of the set point. A seven-metre-long coil array, with transverse positions at x_i = 0, ±19.5, ±39.0, ±58.5 mm, and two 470-mm-long rotating coil segments are employed.

The measurements used to compare the legacy and the current operational MD1 cycles are the following: A = legacy 200 GeV MD1 (peak 2340 A), B = flattened 26 GeV MD1 (peak 300 A), each consisting of twenty identical MD1 cycles.Ten standardisation pre-cycles to 5780 A (LHC cycles) precede each supercycle, and after the MD1 cycle, an SFTPRO cycle (peak 4820 A) is executed.

Figure 1 shows the two supercycles compared in this work.

Eddy-Current Characterisation

The post-ramp settling of the magnetic field measured by the long search coil is fitted as [8] $B(t) = B_\infty +$

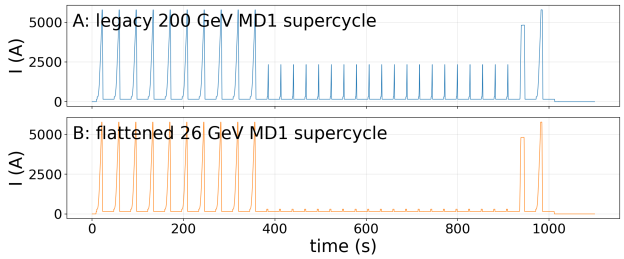

Figure 1: The two MD1 supercycles. Both start with ten LHC pre-cycles to 5780 A, then play twenty MD1 cycles — A (top): legacy 2340 A peak; B (bottom): flattened 300 A peak — followed by the SFTPRO cycle (peak 4820 A) and a final LHC cycle.

$\sum_{i=1}^{N} a_i\, e^{-t/\tau_i}$, where B_∞ is the asymptotic field value after full settling and a_i, τ_i are the amplitude and time constant of mode i, respectively.

A sensitivity analysis of the fit window and model orders 1–4 was conducted to identify the best-fitting window and order. The best-fitting order is three at every current and branch that was studied.

Static B_1, b_2 and b_3

The static field profile is measured at the end of dedicated plateaus at I = 250, 1000, 2500, and 4900 A, after all three eddy-current modes characterised in the previous subsection have decayed below the integrated-drift floor (about $\geq 10\,\tau_{\text{slowest}}$ past the ramp end). For each plateau, the search coils yield flux integrals $\Delta\Phi_i = \int V_i\, dt$ at different transverse positions. A polynomial fit, $\Delta B(x) = \Delta B_1 + \Delta B_2\,(x/R_{\text{ref}}) + \cdots + \Delta B_5\,(x/R_{\text{ref}})^4$, is performed on the per-coil field changes $\Delta B(x_i) = \Delta\Phi_i / N A_{\text{coil\_i}}$, and the normalised multipoles are $b_n = (\Delta B_n/\Delta B_1) \times 10^4$ [9].

METROLOGICAL CHARACTERISATION

The performance of the measurement chain is summarised in Table 1. The voltage noise floor on shorted channels sets the floor for resolving slow-eddy components ($A_i \sim 100\,\mu\text{V s}$ over 10 s). The integration drift rate after constant-baseline subtraction [10, 11] is reported as a single figure of merit, obtained by averaging the median drift/window length over $T \in \{1, 5, 10, 20\}$ s and across the four plateau currents on the seven integral coils.

Table 1: Measured Performance of the Measurement Chain

Quantity	Value
Integrated drift rate	$0.8 \pm 0.1\ \mu\text{T s}^{-1}$
Sample rate	100 kHz
Session-to-session reproducibility of $\int V\, dt$ (SFTPRO ramp, central coil)	$\sigma \approx 10\,\mu\text{T}$ per session
Converter reproducibility	0.03 % of set-point

RESULTS AND DISCUSSION

A current ramp to a plateau reveals three physically distinct regimes, which we treat in turn. *During the ramp*, the field follows a hysteresis loop whose initial state is determined by the previous excitation history, while its width increases with dI/dt due to induced current dissipation. *At the end-of-ramp transient*, the field relaxes towards its plateau value through a superposition of eddy-current modes that are mainly dependent on the saturation state of the iron. *At the end of the plateau*, after all eddy-current modes have decayed below the noise floor, the field is rate-independent and uniquely set by the iron's hysteresis state.

Dynamic B_1: Study of the Flattened MD1 Cycle

The A–B difference along the SFTPRO ascending ramp, averaged over the eight sessions arranged in an A-B-B-A pattern, is shown in Fig. 2 and summarised in Table 2.

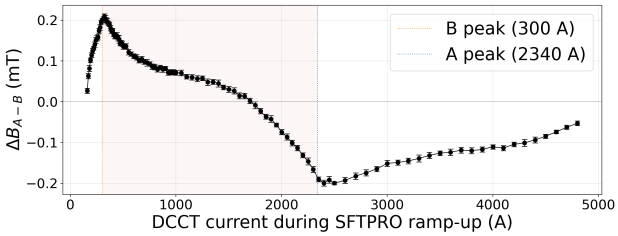

Figure 2: A–B field difference along the SFTPRO ascending ramp on the central coil of the fluxmeter, averaged over the four A and four B sessions. Error bars are the $\pm 1\sigma$ standard error of the mean across sessions; vertical dotted lines mark the B-session (300 A) and A-session (2340 A) MD1 peaks.

Table 2: A–B Differences Along the SFTPRO Ascending Ramp

I (A)	ΔB_1^{A-B} (mT)
155 (idle, pre)	±0.01
300	+0.20
1000	+0.10
1500	−0.01
2340	−0.21
4820 (flat top)	−0.05
155 (idle, post)	±0.01

At the flat bottoms before and after the SFTPRO cycle, the A and B sessions agree to ±0.01 mT: regardless of the minor-loop pattern played in between, the LHC pre-cycle that precedes each supercycle resets both branches to the same magnetic state. The SFTPRO flat-top (4820 A) is the operationally critical point of the supercycle, since it sets the field at which protons are slow-extracted to the North Area; any A–B residual there propagates directly to the extracted-beam orbit. At this current, a stable residual $\Delta B_1^{A-B} = -0.05$ mT is reproduced across all eight A-B-B-A sessions, well above the per-session reproducibility of the chain (Table 1).

Between the reversal points, however, the ascending ramp — the field-vs-current trajectory traced after a reversal of

ramp direction, whose shape depends on the iron saturation before [12] — carries a reproducible signature of the prior minor-loop MD1: in the 200 GeV case, the iron (A sessions, 20 minor loops in [155, 2340] A) magnetises more easily at low currents and saturates less near the MD1 peak. The sign-reversing pattern with zero crossing at ∼1500 A is the signature of minor-loop narrowing, an accommodation effect that the classical Preisach model does not capture.

The A–B difference on b_3, extracted at each ramp current from the polynomial fit on the seven integral coils, stays below 0.05 units everywhere along the ramp.

Eddy-Current Settling at the End-of-Ramp Transient

The resulting time constants are reported in Table 3.

Table 3: Eddy-Current Time Constants (MBA)

Branch	I (A)	τ_1 (ms)	τ_2 (ms)	τ_3 (s)
Ramp-up	1000	46 ± 3	359 ± 53	2.9 ± 0.8
Ramp-up	2500	56 ± 3	344 ± 19	2.2 ± 0.4
Ramp-up	4900	61 ± 2	311 ± 29	2.0 ± 0.1
Ramp-down	4900	61 ± 7	431 ± 65	2.8 ± 0.4

For SPS MBA dipoles, the time constant of eddy currents in the laminated yoke, if estimated from an analytical model as $\tau_{\mathrm{lam}} \approx 26\,\mu$s, is below our analysis resolution and therefore invisible. The same applies to the vacuum-chamber eddy-current time constant: the thin-tube formula [13] gives a chamber eddy-current time constant $\tau_{\mathrm{vc}} \sim 60\,\mu$s, comparable to the lamination one.

The three modes we have identified resolve in greater detail earlier observations ($\tau \approx 100$ ms [14]) and beam-based measurements ($\tau \approx 850$ ms [15]), and provide reference data for data-driven models of normal-conducting accelerator magnets [16, 17].

Static B_1, b_2 and b_3 at the Plateau

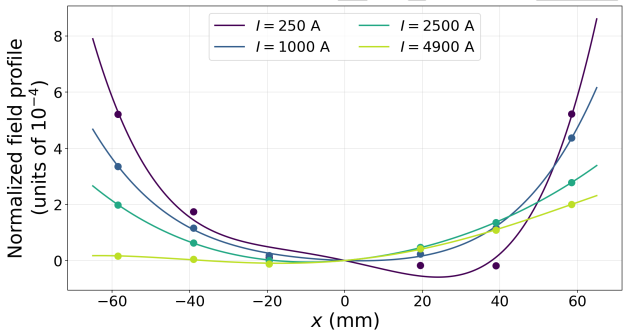

Figure 3: Normalised static field profile $[\Delta B(x)/\Delta B(0) - 1] \times 10^4$ at the four plateau currents. Line: 4th-order polynomial fit on the integral coils.

Figure 3 shows the static field profiles at the four plateau currents with the 4th-order polynomial fit on the integral coils, and Table 4 reports the resulting multipoles b_2, b_3 together with the transfer function $\Delta B_1/I$; the higher orders b_4, b_5 stay below 0.05 units of 10^{-4} across the four currents and are dropped for brevity.

Table 4: Transfer Function and Multipoles at $R_{\mathrm{ref}} = 13$ mm

I (A)	$\Delta B_1/I$ (T/kA)	b_2	b_3
250	0.3328	−0.38	−0.05
1000	0.3346	−0.05	+0.08
2500	0.3348	+0.15	+0.11
4900	0.3229	+0.16	+0.07

The transfer function $\Delta B_1/I$ is flat to within 0.5 % between 250 A and 2500 A and drops by ∼3.5 % at 4900 A — the saturation tail of the iron, deepening further at the 5780 A reached on the LHC pre-cycle. The sextupole shows a non-monotonic dependence on current: b_3 rises from −0.05 at 250 A to a peak of +0.11 near 2500 A and falls back to +0.07 at 4900 A, as pole-tip saturation progressively redistributes the iron contribution across the aperture. This trend is consistent in sign and shape with the change-from-idle Δb_3 extracted from the SFTPRO ascending ramp discussed above. The quadrupolar component b_2 crosses zero between 1000 A and 2500 A, reflecting the same redistribution.

CONCLUSION AND OUTLOOK

A magnetic characterisation of an SPS dipole was carried out using a new seven-metre-long integral-coil fluxmeter, designed and developed in-house, and employed in its first measurement campaign on an MBA dipole under operational supercycles.

The measurements show that the legacy and flattened MD1 pre-cycles return to a similar magnetic state at the start of the next ramp. At the operationally critical SFTPRO flattop, flattening the MD1 pre-cycle introduces a systematic difference, as shown in Figure 2.

Although this difference is small, at both flat-bottom and flat-top it peaks during the ramp at about 0.2 %.

The end-of-ramp transient is decomposed into three exponential modes, reconciling the order-of-magnitude scatter among previously reported results.

The static transfer function is flat across most of the operational range and drops at the highest currents as the iron approaches saturation, with a non-monotonic sextupole and a quadrupole that crosses zero in the same range, both consistent with progressive pole-tip saturation.

The next step is to extend these measurements to additional cycle families and supercycle compositions across the SPS operational cycles, and to bridge single-magnet bench data, B-train integrated measurements, and beam observables (orbit, tune, chromaticity) into a unified framework.

REFERENCES

[1] R. Alemany Fernandez *et al.*, *Summary Report of the Physics Beyond Colliders Initiative*, Rep. CERN-PBC-REPORT-2025-003, CERN, Geneva, Switzerland, 2025. https://cds.cern.ch/record/2927631

[2] C. Grech *et al.*, "Development of a real-time magnetic field measurement system for synchrotron control," *Electronics*, vol. 10, no. 17, p. 2140, 2021. doi:10.3390/electronics10172140

[3] C. Grech, R. Avramidou, A. Beaumont, M. Buzio, N. Sammut, and J. Tinembart, "Metrological characterization of nuclear magnetic resonance markers for real-time field control of the CERN ELENA ring dipoles," *IEEE Sensors J.*, vol. 18, no. 14, pp. 5826–5833, 2018. doi:10.1109/JSEN.2018.2842710

[4] A. Lu, V. Kain, C. Petrone, V. Di Capua, M. Schenk, and M. Taupadel, "Data-driven hysteresis compensation in the CERN SPS main magnets," in *Proc. 16th Int. Particle Accelerator Conf. (IPAC'25)*, Taipei, Taiwan, Jun. 2025, pp. 1674–1677, paper WEAN2. doi:10.18429/JACoW-IPAC2025-WEAN2

[5] A. Lu and V. Kain, "Transformers for deterministic magnetic field control in particle accelerators," in *Machine Learning and the Physical Sciences Workshop, NeurIPS 2025*, Dec. 2025. https://ml4physicalsciences.github.io/2025/files/NeurIPS_ML4PS_2025_241.pdf

[6] E. Shaposhnikova, "Lessons from SPS studies in 2010," in *Proc. Chamonix 2011 Workshop on LHC Performance*, Chamonix, France, Jan. 2011, pp. 359–365. https://cds.cern.ch/record/1353880

[7] H. Bartosik *et al.*, "SPS operation and future proton sharing scenarios for the SHiP experiment at the BDF facility," CERN, Geneva, Switzerland, Rep. CERN-ACC-NOTE-2018-0082, CERN-PBC-Notes-2021-008, Dec. 2018. https://cds.cern.ch/record/2650722

[8] M. Buzio, "Measurement and control of dynamic effects," lecture slides, CAS – CERN Accelerator School: Normal- and Superconducting Magnets, St. Pölten, Austria, Nov. 2023. https://indico.cern.ch/event/1227234/contributions/5601210/

[9] S. Russenschuck, *Field Simulation for Accelerator Magnets*. Weinheim, Germany: Wiley, 2025. doi:10.1002/9783527839599

[10] M. Amodeo, P. Arpaia, and M. Buzio, "Integrator drift compensation of magnetic flux transducers by feed-forward correction," *Sensors*, vol. 19, no. 24, p. 5455, 2019. doi:10.3390/s19245455

[11] P. Arpaia, M. Buzio, V. Di Capua, S. Grassini, M. Parvis, and M. Pentella, "Drift-free integration in inductive magnetic field measurements achieved by Kalman filtering," *Sensors*, vol. 22, no. 1, p. 182, 2022. doi:10.3390/s22010182

[12] I. D. Mayergoyz, *Mathematical Models of Hysteresis and their Applications*, 2nd ed., Amsterdam, The Netherlands: Elsevier, 2003. doi:10.1016/B978-0-12-480873-7.X5000-2

[13] G. Moritz, "Eddy currents in accelerator magnets," in *Proc. CAS – CERN Accelerator School: Magnets*, Bruges, Belgium, Jun. 2009, CERN-2010-004, pp. 103–140. doi:10.5170/CERN-2010-004.103

[14] M. Buzio, R. Chritin, and D. Giloteaux, "Measurement of the inductance of resistive magnets: two case studies," CERN, Geneva, Switzerland, Tech. Note CERN-ATS-Note-2011-047 TECH, EDMS 1148084, Jun. 24, 2011. https://cds.cern.ch/record/1361317

[15] C. Arimatea, D. Jacquet, L. Normann, and J. Wenninger, "Dipole field, tune and chromaticity correction at the SPS: from converter tracking to eddy currents," CERN, Geneva, Switzerland, Tech. Note CERN-AB-Note-2007-009, Jan. 2007. https://cds.cern.ch/record/1014025

[16] S. Sorti, C. Petrone, S. Russenschuck, and F. Braghin, "Data-driven simulation of transient fields in air-coil magnets for accelerators," *Nucl. Instrum. Methods Phys. Res. A*, vol. 1011, p. 165571, 2021. doi:10.1016/j.nima.2021.165571

[17] S. Sorti, C. Petrone, S. Russenschuck, and F. Braghin, "Data-driven modelling of nonlinear materials in normal-conducting magnets," *Phys. Rev. Accel. Beams*, vol. 25, p. 052401, 2022. doi:10.1103/PhysRevAccelBeams.25.052401